Low-strain effective Young's modulus model and validation for multi-layer vocal fold-based silicone specimens with inclusions EP

M. Ahmad,[1] ID X. Pelorson,[1] I. A. Fernández,[2] ID O. Guasch,[3] ID and A. Van Hirtum[1,a) ID

AFFILIATIONS

[1]Univ. Grenoble Alpes, CNRS, Grenoble INP, LEGI, 38000 Grenoble, France
[2]Department of Materials Science and Physical Chemistry, University of Barcelona, 8001 Barcelona, Spain
[3]Department of Engineering, La Salle, Universitat Ramon Llull, 8001 Barcelona, Spain

[a)]**Author to whom correspondence should be addressed:** annemie.vanhirtum@univ-grenoble-alpes.fr

ABSTRACT

A model of the effective low-strain elastic Young's modulus of multi-layer stacked composites is proposed, which is capable to account for an arbitrary stacked inclusion. Geometrical and discretization-based model results are validated against measured effective Young's moduli (from 10 up to 40 kPa) on 14 molded silicone specimens embedding a stiff (298 kPa) inclusion with variable size, position, and stacking. Specimens without inclusion represent the muscle, superficial, and epithelium layers in a human vocal fold with Young's moduli between 4 and 65 kPa. The proposed model allows to predict the influence of a stiff inclusion, mimicking a structural abnormality or pathology somewhere within the vocal fold, on the low-strain effective Young's modulus. Quantifying the influence of an inclusion or local stiffening on the vocal fold bio-mechanics is a necessary step toward the understanding and mitigation of structural vocal fold pathologies and associated voice disorders.

Published under an exclusive license by AIP Publishing. https://doi.org/10.1063/5.0080468

I. INTRODUCTION

Phonation or voiced speech sound production is due to the fluid–structure interaction (FSI) between the airflow coming from the lungs along the inferior–superior direction and the vocal fold tissues enveloping the airflow within the glottis.[1] Although the physical mechanisms driving phonation are known,[2–4] systematic studies of the influence of the vocal folds' structure, either normal or abnormal, on the FSI and subsequent vocal fold auto-oscillation are few[5,6] as most physical studies focus on the glottal flow.[7–9] This is partly due to the lack of a low-cost computational model predicting the elasticity of deformable silicone vocal fold replicas mimicking, up to some extent, the multi-layer (ML) anatomical representation[1] of a human vocal fold without (Fig. 1) or with structural abnormality or pathology.

In the linear low-strain region, the stress–strain relationship is described by Hooke's law so that the elasticity of a soft material is characterized by its low-strain or elastic Young's modulus. In Ref. 10, a quasi-analytical model of the low-strain effective elastic Young's modulus $\mathcal{E}_{eff}$ was proposed for homogenized ML silicone composites with serial ($\perp$), parallel ($\parallel$), or combined ($\perp\parallel$) stacked layers with respect to the force direction, as depicted in Fig. 2. This means that composites are treated as n layers that are stacked either serial or parallel to each other. The model was validated (overall accuracy of ± 2.4 kPa) against measured $\mathcal{E}_{eff}$ from uni-axial tensile tests at room temperature $21 \pm 2\,°C$ using precision loading (PL) and a mechanical press. The validation was done on 13 bone-shaped molded silicone specimens containing two ($\perp$ or $\parallel$) or three ($\perp$, $\parallel$, or $\perp\parallel$) layers and $\mathcal{E}_{eff} \le 40$ kPa. Young's modulus $\mathcal{E}$ of the molded layers was varied considering two different silicone mixtures [Thinner-Ecoflex (TE) or Thinner-Dragonskin (TD)] at different mass mixing ratios $\mathcal{M} = r_T : r_{E(D)}$ with constant $r_{E(D)} = 2$. Silicone mixtures, mixing ratios $\mathcal{M}$, and measured $\mathcal{E}$ commonly used to represent the muscle (Mu), superficial (Su), and epithelium (Ep) layers in ML silicone vocal fold replicas are given in Table I.[10–18] The measured Young's modulus $\mathcal{E}$ of molded layers varies between 4 and 65 kPa, which corresponds to the range associated with anatomical layers in a normal adult male human vocal fold.[19–25]
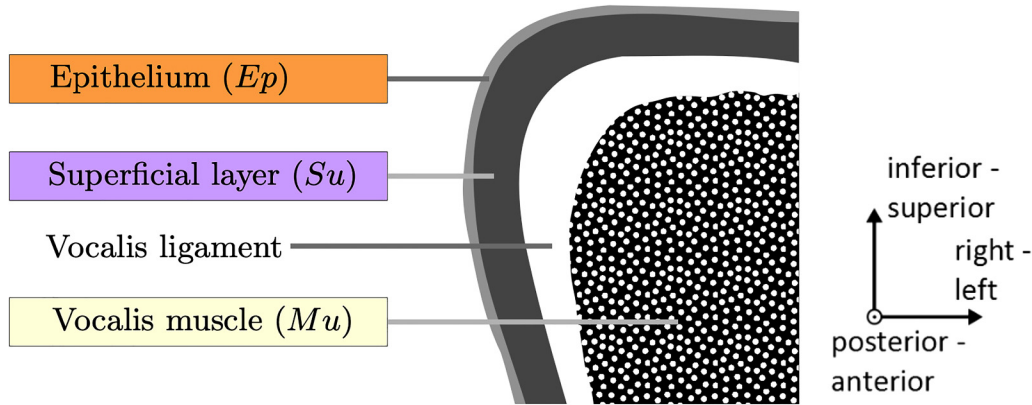
FIG. 1. Multi-layer representation of the anatomical structure of a human vocal fold in the medio-frontal plane, i.e., a coronal section.

The current work aims to propose a model approach predicting $\mathcal{E}_{eff}$ for a multi-layered specimen containing a stiff inclusion. The model outcome is validated against uni-axial tensile test measurements (using precision loading[10]) on molded bone-shaped composite specimens. All experiments are done at room temperature, $21 \pm 2\,^\circ$C. Specimens are obtained from a three-layer reference specimen (labeled $A_{0.0}$) to which a stiffer silicone inclusion (In) is inserted with constant elasticity $\mathcal{E}^{In}$ as given in Table I. The reference specimen without inclusion is depicted in Fig. 3. It consists of three serial ($\perp$) stacked layers with a composition similar to the muscle, superficial, and epithelium layers as indicated in Table I. The length l_i of each layer $i = 1 \ldots n$ in the force ($\mathcal{F}$) direction, with $n = 3$ serial stacked layers, is set so that the volume ratios for the muscle, superficial, and epithelium layers with respect to the test section's volume match the volume ratios of a three-layer silicone vocal fold replica (MRI-replica[14,16–18]), i.e., 69% (Mu, $i = 1$), 27% (Su, $i = 2$), and 4% (Ep, $i = 3$), respectively. The size, the position, or the orientation of the inclusions is varied resulting in complex ML composites. From the ratio $\mathcal{E}^{In}/\mathcal{E}$ in Table I, it is seen that $\mathcal{E}^{In}$ is about 4.5 up to 75 times greater than $\mathcal{E}$ associated with the layers in $A_{0.0}$. The presence of a stiffer portion somewhere within the vocal fold structure is commonly reported in the case of a vocal fold abnormality or pathology.[1,26–28] Consequently, a validated model is sought for ML specimens embedding a stiffer inclusion, for which besides Young's modulus also the size, position, and stacking orientation are varied. This will contribute
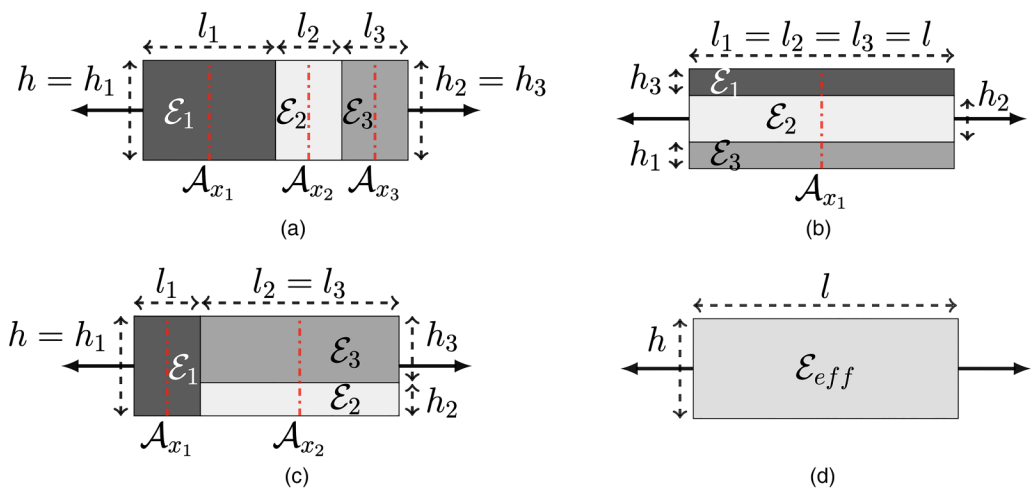

FIG. 2. Layer stacking with respect to the force direction (black arrows) for three-layer ($n = 3$) composites with height h and length l: (a) serial ($\perp$), (b) parallel ($\parallel$), (c) combined ($\perp\parallel$), and (d) sought homogenized composite with effective Young's modulus $\mathcal{E}_{eff}$. Layers Young's moduli $\mathcal{E}_i$ and dimensions (height h_i, length l_i) are indicated with $i = 1 \ldots n$. Positions of midway cross section area measurements $\mathcal{A}_{x_s}$ are indicated (dashed-dotted line) for each serial stacked equivalent layer $s = 1 \ldots k$ so that in (a) $k = 3$, (b) $k = 1$, and (c) $k = 2$. (a) Serial $\perp$, (b) parallel $\parallel$, and (c) combined $\perp\parallel$, and (d) homogenized.

TABLE I. Molded layer properties: mixture (Mix) TE (Thinner-Ecoflex) or TD (Thinner-Dragonskin), mass mixing ratio $\mathcal{M}$, measured Young's modulus $\mathcal{E}$, and ratio between $\mathcal{E}$ and the value of the inclusion $\mathcal{E}^{In}$.

Molded layer	Mix	$\mathcal{M}$ [-]	$\mathcal{E}$ [kPa]	$\mathcal{E}^{In}/\mathcal{E}$ [-]
Muscle (Mu)	TE	1:2	23	13.0
Superficial (Su)	TE	4:2	4	74.5
Epithelium (Ep)	TD	1:2	65	4.6
Inclusion (In)	TD	0:2	298[a]	1.0

[a]$\mathcal{E}$ of the inclusion material is denoted $\mathcal{E}^{In}$.

to the systematic prediction and understanding of the effect of an inclusion on the low-strain elasticity of silicone ML vocal fold replicas mimicking a local vocal fold structural abnormality or pathology.

Concretely, six specimen types (resulting in 15 molded specimens) are experimentally assessed in order to complete the model validation with respect to the main inclusion characteristics: position, size (length and height), and shape. This validation is pertinent to the representation with silicone-based vocal fold replicas of vocal fold pathologies characterized by an arbitrary-shaped inclusion of any size embedded somewhere within a single or multiple vocal fold layers. The specimen types with inclusions are presented in Sec. II. Molded specimens are motivated. Next, the measurement of low-strain effective Young's moduli for the molded specimens is detailed in Sec. III. The analytical model approach for the effective Young's modulus of ML composite specimens with an inclusion and serial, parallel, or combined stacking is outlined in Sec. IV. A discretization and geometrical based model approach for arbitrary stacked layers is proposed. Measured and modeled effective Young's moduli for different inclusions are discussed in Sec. V. The conclusion is formulated in Sec. VI.

II. MOLDED SPECIMENS WITH INCLUSION

Figure 4 schematically illustrates the different positions of beam-shaped inclusions with varying height h_{in} and length l_{in}
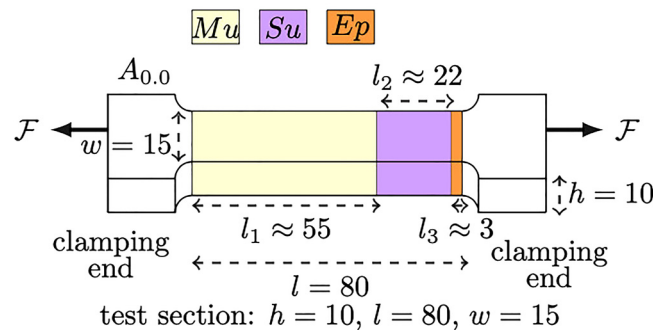

FIG. 3. Molded bone-shaped three-layer reference specimen $A_{0.0}$ with serial stacking ($\perp$) without inclusion (dimensions in mm). The force $\mathcal{F}$ direction during uni-axial tension testing is shown (black arrows).
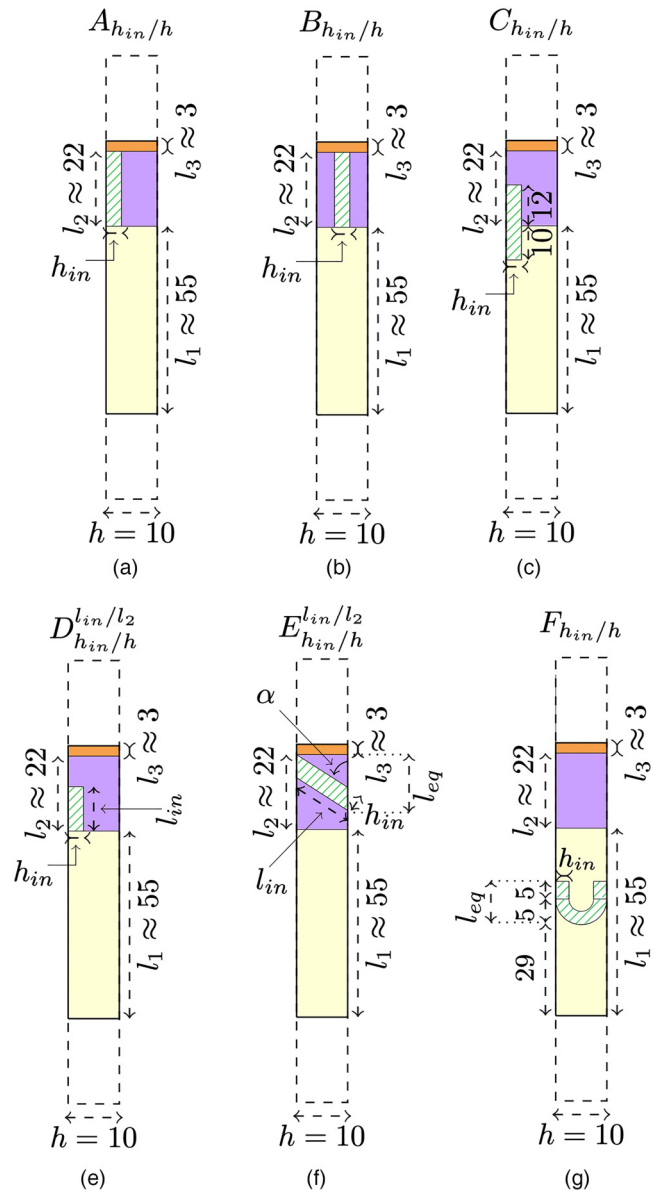

FIG. 4. Side view of molded ML composite types with inclusions (striped region) of size h_{in}, l_{in}, and constant width $w_{in} = 15$ mm (dimensions in mm). In (a), (b), (c), and (f), $l_{in} = l_2$. In (d) and (e), $l_{in} < l_2$. The clamping ends are dashed. (a) Type A, (b) type B, (c) type C, (d) type D, (e) type E, and (f) type F.

inserted (striped region) in the test section of the reference specimen $A_{0.0}$ with serial layer stacking ($\perp$) as depicted in Fig. 3. All inclusions have constant width $w_{in} = 15$ mm, which matches the width of the test section ($w_{in} = w$ with $w = 15$ mm) as illustrated for two specimens with inclusions in Fig. 5. Thus, the inclusion size is fully characterized by its height h_{in} and its length l_{in}, and its position is fully defined by the side views provided in Fig. 4. Six
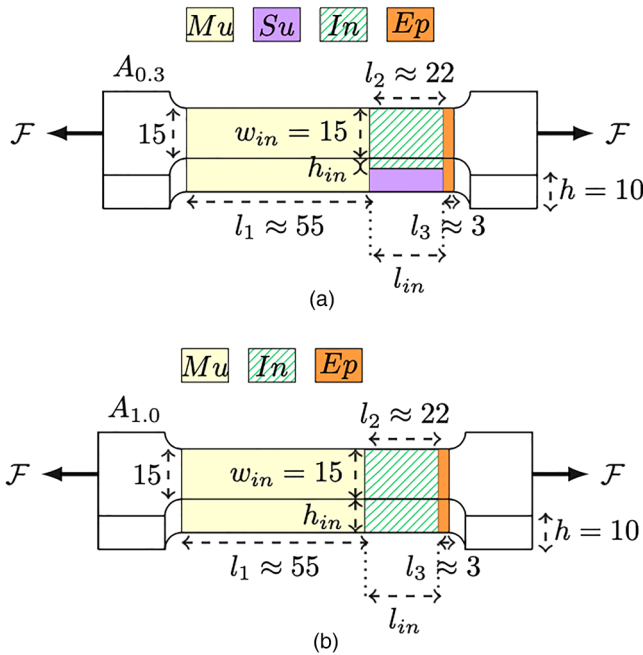
FIG. 5. Molded ML bone-shaped specimens (dimensions in mm) with inclusion (In) inserted in the superficial (Su) layer of the reference specimen $A_{0.0}$ depicted in Fig. 3: (a) Four-layer specimen $A_{0.3}$ with combined stacking ($\perp\|$) and (b) three-layer specimen $A_{1.0}$ with serial stacking ($\perp$). The force $\mathcal{F}$ direction during uni-axial tension testing is shown (black arrows). (a) $A_{0.3}$ and (b) $A_{1.0}$.

different ML composite specimen types—A, B, C, D, E, and F—are considered based on the position and size of the inclusion. Concretely, the size, in terms of height h_{in} and length l_{in}, of experimentally assessed inclusions is summarized in Table II:

TABLE II. Inclusions geometry (constant width $w_{in} = 15$ mm): h_{in}, l_{in}, and ratios h_{in}/h and l_{in}/l_2 with $h \approx 10$ mm and $l_2 \approx 22$ mm. ML molded specimens with these inclusions and their layer stacking: serial ($\perp$), combined ($\perp\|$), and arbitrary (Arb). Reference specimen $A_{0.0}$ corresponds to $h_{in}/h = 0$.

Inclusion geometry		Dimension ratios		Specimens and stacking		
h_{in} (mm)	l_{in} (mm)	h_{in}/h (-)	l_{in}/l_2 (-)	($\perp$)	($\perp\|$)	Arb
0.0	…	0.0	0.0	$A_{0.0}$		
1.3	22.0	0.1	1.0		$A_{0.1}$ $B_{0.1}$	
2.6	22.0	0.3	1.0		$A_{0.3}$ $B_{0.3}$	$F_{0.3}$
5.8	22.0	0.6	1.0		$A_{0.6}$ $B_{0.6}$	
7.8	22.0	0.8	1.0		$A_{0.8}$ $C_{0.8}$	
10.0	22.0	1.0	1.0	$A_{1.0}$		
2.6	5.0	0.3	0.2		$D_{0.3}^{0.2}$	
7.8	5.0	0.8	0.2		$D_{0.8}^{0.2}$	
4.6	13.4	0.5	0.6		$D_{0.5}^{0.6}$	$E_{0.5}^{0.6}$

(A) Specimens $A_{h_{in}/h}$ [Fig. 4(a)] are obtained for five inclusions with constant length $l_{in} = l_2$ and varying height $0.1 \leq h_{in}/h \leq 1$ placed at the side of the superficial layer (Su, $i = 2$) of $A_{0.0}$. In general, these specimens have four layers ($n = 4$) with combined stacking ($\perp\|$) as the inclusion in the superficial layer results in two adjacent layers with parallel stacking. This is illustrated for $A_{0.3}$ ($h_{in}/h = 0.3$) in Fig. 5(a). In the extreme case, that the inclusion replaces the superficial layer ($h_{in}/h = 1.0$), a three-layer ($n = 3$) specimen $A_{1.0}$ with serial stacking ($\perp$) is obtained as illustrated in Fig. 5(b).

(B) Specimens $B_{h_{in}/h}$ [Fig. 4(b)] are obtained for three of the five inclusions with constant length $l_{in} = l_2$ and varying height $0.1 \leq h_{in}/h \leq 0.6$ considered in type A, but now translated (in the transverse direction) to the center of the superficial layer (Su, $i = 2$) in $A_{0.0}$. Comparing the elasticity of $A_{h_{in}/h}$ and $B_{h_{in}/h}$ allows to assess the influence of the transverse inclusion position (side vs center) within the superficial layer of $A_{0.0}$. These specimens are composed of five layers ($n = 5$) with combined stacking ($\perp\|$) as the inclusion in the superficial layer results in three adjacent parallel stacked layers.

(C) Specimen $C_{h_{in}/h}$ [Fig. 4(c)] is obtained using the inclusion with constant length $l_{in} = l_2$ and height $h_{in}/h = 0.8$ positioned in both the superficial and the muscle layers of $A_{0.0}$. This specimen can be considered as a seven-layer ($n = 7$) specimen with combined stacking ($\perp\|$) as the inclusion has parallel stacking with respect to the adjacent portions of the superficial layer and the muscle layer.

(D) Specimens $D_{h_{in}/h}^{l_{in}/l_2}$ [Fig. 4(d)] are obtained for five inclusions with varying length $0.2 \leq l_{in}/l_2 \leq 0.6$ and varying height $0.3 \leq h_{in}/h \leq 0.8$ placed at the side of the superficial layer and at the interface with the muscle layer. These specimens are considered to have five layers ($n = 5$) with combined stacking ($\perp\|$) as the inclusion has a parallel stacking with respect to the adjacent portion of the superficial layer with the same height. Thus, the inclusion length is reduced so that comparing type A and type D allows one to assess the influence of the inclusion length.

(E) Specimen $E_{h_{in}/h}^{l_{in}/l_2}$ [Fig. 4(e)] is obtained by inclining the inclusion with angle α ($\alpha = 46°$ is experimentally assessed). The inclined inclusion is placed in the superficial layer at the interface with the epithelium layer. Due to inclination, the stacking in the superficial layer is arbitrary (Arb) and it is neither serial ($\perp$) nor parallel ($\|$) with respect to the adjacent superficial layer portion. The equivalent length l_{eq} of the inclusion corresponds to its length in the force direction and $l_{eq} < l_{in}$ due to the inclination.

(F) Specimen $F_{h_{in}/h}$ [Fig. 4(f)] is obtained by bending the inclusion with length $l_{in} = l_2$ and placing it in the muscle layer. As for type E, the stacking orientation within the muscle layer is arbitrary (Arb) since the bent portion of the inclusion is stacked neither serial ($\perp$) nor parallel ($\|$) with respect to the adjacent muscle layer portion. Again, the equivalent length l_{eq} of the inclusion corresponds to its length in the force direction and $l_{eq} < l_{in}$ due to bending.

A total of 15 silicone specimens are molded following the mixture procedure outlined in Refs. 29 and 10. The size and position of the inclusion and the resulting ML specimen type (Fig. 4)

and associated layer stacking—serial ($\perp$), combined ($\perp\|$), or arbitrary (Arb)—are summarized in Table II. First, inclusions are molded using horizontal 3D-printed specimen molds (Stratasys ABS-P430, accuracy 0.33 mm), which are filled with the inclusion silicone mixture indicated in Table I up to each inclusion's height h_{in}, whereas their width is determined by the width of the mold so that $w_{in} = 15$ mm. The molded inclusion sheets are then cut to match the desired inclusion length l_{in}. Next, vertical 3D-printed specimen molds are used to build the ML specimens layer-by-layer with the appropriate silicone mixture detailed in Table I. Inclusions are inserted during the molding process so that they are fully embedded. The length of each molded layer is measured with a laser transceiver (Panasonic HL-G112-A-C5, wavelength 655 nm, accuracy 8 μm), whereas the inclination angle is derived from the spatial position of the inclined mold (accuracy 0.1 mm) using trigonometry. The overall molding accuracy for all 45 molded layers with lengths $l_1 \approx 55$ mm (muscle), $l_2 \approx 22$ mm (superficial), and $l_3 \approx 3$ mm (epithelium) results in a mean and a standard deviation of 0.1 ± 0.8 mm, which is within the molding accuracy of ± 1.5 mm previously reported.[10]

III. UNI-AXIAL TENSION TESTS AND $\mathcal{E}_{eff}$ ESTIMATION

A. Uni-axial tension test data on molded specimen

In order to experimentally estimate the linear or low-strain effective Young's moduli $\mathcal{E}_{eff}$ of the 15 molded composite specimens, uni-axial tension tests using precision loading (PL) are performed.[10] First, the tested specimen is placed vertically and fixed from one clamping end. Then, a weight of mass m (Vastar 500G X 0.01G, accuracy 0.01 g) is added to the other clamping end in order to control the force increment. The weight is increased at a single rate for each specimen. Overall, i.e., considering all specimens, the weight is incremented with 10.9~(6.9) g [mean (and standard deviation)]. Total added weight ranges from 46.8 to 425.9 g, resulting in a total applied loading force $\mathcal{F}$ ranging from 0.5 to 4.2 N. The applied force $\mathcal{F}$ causes an elongation Δl_s of each equivalent serial stacked layer with initial length l_s. The total elongation $\Delta l = \sum_{s=1}^{k} \Delta l_s$ is then measured at every added weight increment with an accuracy of 0.05 mm, where k indicates the number of equivalent serial stacked layers. Total elongation measured for all specimens

ranges from 23.0 up to 131.0 mm. From these measurements, force-elongation relationship $\mathcal{F}(\Delta l)$ can be obtained. Examples of two force-elongation diagrams for two different specimens $A_{0.0}$ and $A_{0.8}$ are plotted in Fig. 6(a). Additionally, the midway cross-sectional area of each equivalent serial stacked layer $\mathcal{A}_{x_s}$ perpendicular to the forcing direction is measured with an accuracy of 0.02 mm as illustrated in Fig. 2. For each specimen, cross-sectional areas $\mathcal{A}_{x_s}$ are measured at a constant weight increment amounting to 26.7 ± 15.9 g for all specimens, which corresponds to an elongation increment of 10.6 ± 4.5 mm. The specimen cross-sectional area $\mathcal{A}$ is then calculated from the arithmetic mean of its measured cross-sectional areas weighted by their respective lengths as

$$\mathcal{A} = \frac{\sum_{s=1}^{k} (l_s + \Delta l_s) \mathcal{A}_{x_s}}{l + \Delta l}. \quad (1)$$

A quadratic fit (coefficient of determination $R^2 \geq 99\%$) to the area-elongation data $\mathcal{A}(\Delta l)$ is then used in order to have a continuous approximation of the area-elongation relationship $\mathcal{A}^q(\Delta l)$ for each specimen. An example of resulting data points $\mathcal{A}(\Delta l)$ and their continuous fit $\mathcal{A}^q(\Delta l)$ for two different specimens $A_{0.0}$ and $A_{1.0}$ is plotted in Fig. 6(b).

B. Experimental $\mathcal{E}_{eff}$ estimation from tensile test data

In order to estimate the linear low-strain effective Young's modulus $\mathcal{E}_{eff}$ for each specimen, stress–strain curves $\sigma_t(\varepsilon_t)$ are first calculated from the measured instantaneous elongation Δl and associated force $\mathcal{F}(\Delta l)$ and area $\mathcal{A}^q(\Delta l)$. The true stress σ_t and true strain ε_t are then given as

$$\sigma_t = \frac{\mathcal{F}}{\mathcal{A}^q}, \quad (2)$$

$$\varepsilon_t = \ln\left(\frac{l + \Delta l}{l}\right). \quad (3)$$

The sought $\mathcal{E}_{eff}$ is obtained by fitting the low-strain region of the stress–strain curves to a linear model whose slope equals $\mathcal{E}_{eff}$, as the relationship between stress and low-strain is governed by Hooke's law,

$$\mathcal{E}_{eff} = \frac{\sigma_t}{\varepsilon_t}. \quad (4)$$

For each specimen, the low-strain region is determined as the range for which R^2 is maximum, where $R^2 \geq 98\%$ expresses the goodness of fitting a linear model to the stress–strain curve with a lower bound at $\varepsilon_t = 0$. For all specimens tested, the mean (and standard deviation) of the upper bound of the low-strain region is $\varepsilon_t = 0.26$ (0.02), which corresponds to a total elongation of 24.5 (1.7) mm. Examples of fitting a linear model to a low-strain region are plotted in Fig. 7 for three different specimens. Figure 7(a) shows the different fits and, hence, slopes $\mathcal{E}_{eff}$, obtained for two specimens $A_{0.0}$ and $A_{0.6}$, without and with an inclusion, respectively. Figure 7(b) shows similar fits and, hence, slopes $\mathcal{E}_{eff}$, obtained for two specimens $A_{0.6}$ and $B_{0.6}$ with the same inclusion ($h_{in}/h = 0.6$ and $l_{in}/l_2 = 1$) but positioned at either the side ($A_{0.6}$) or the center ($B_{0.6}$) of the superficial layer in $A_{0.0}$.
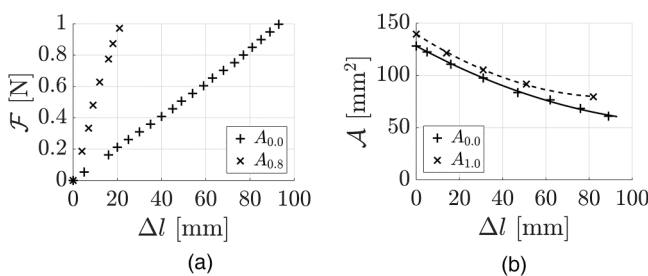

FIG. 6. Examples of uni-axial tension testing data: (a) Force-elongation data $\mathcal{F}(\Delta l)$ for specimens $A_{0.0}$ and $A_{0.8}$ with $m \leq 102$ g and $m \leq 231$ g, respectively; (b) area-elongation data $\mathcal{A}(\Delta l)$ and quadratic fits $\mathcal{A}^q(\Delta l)$ with $R^2 = 99\%$ (lines) for specimens $A_{0.0}$ and $A_{1.0}$. (a) $\mathcal{F}(\Delta l)$ and (b) $\mathcal{A}(\Delta l)$.
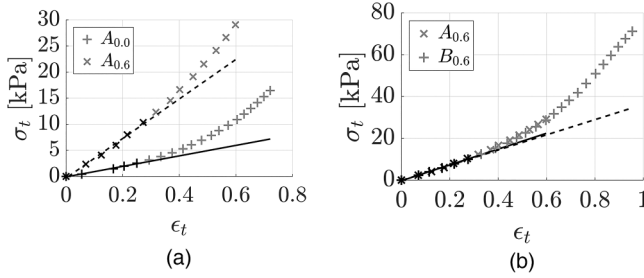
FIG. 7. Experimental stress–strain curves $\sigma_t(\epsilon_t)$ for three specimens and linear fits (lines) to the low-strain region ($R^2 \geq 98\%$) with slope $\mathcal{E}_{eff}$: (a) Specimens $A_{0.0}$ and $A_{0.6}$ (low-strain region $\varepsilon_t \leq 0.25$ and $\varepsilon_t \leq 0.27$) and (b) specimens $A_{0.6}$ and $B_{0.6}$ (low-strain region $\varepsilon_t \leq 0.27$). (a) Size and (b) position.

IV. EFFECTIVE YOUNG'S MODULUS $\widehat{\mathcal{E}}_{eff}$ MODEL

A. Serial, parallel, and combined layer stacking

For the composite specimens in Table II and in Fig. 4 with serial ($\perp$) or combined ($\perp\parallel$) stacked layers—i.e., of type A [Fig. 4(a)], type B [Fig. 4(b)], type C [Fig. 4(c)], or type D [Fig. 4(d)]—the effective Young's modulus $\widehat{\mathcal{E}}_{eff}$ is modeled considering an equivalent homogeneous composite [e.g., in Fig. 2(d)] as outlined in Ref. 10 for serial, parallel, or combined stacked layers.

For k serial ($\perp$) stacked layers [e.g., in Fig. 2(a)], the Reuss hypothesis of homogeneous stress[30] between the stress in the equivalent homogeneous composite σ and the stress $\sigma_{i=1...k}$ in each layer is applied so that $\sigma = \sigma_{i=1...k}$. The effective Young's modulus of the equivalent homogeneous composite is then obtained as the harmonic mean of the layers' Young's moduli $\mathcal{E}_i$ weighted with their lengths l_i so that

$$\widehat{\mathcal{E}}_{eff}^{\perp} = \frac{\sum\limits_{i=1}^{k} l_i}{\sum\limits_{i=1}^{k}\left(\frac{l_i}{\mathcal{E}_i}\right)}, \tag{5}$$

with $l = \sum_{i=1}^{k} l_i$ being the length of the equivalent homogeneous composite. Equation (5) is independent of the layer order in the serial stack.

For k parallel ($\parallel$) stacked layers [e.g., in Fig. 2(b)], the Voigt hypothesis of homogeneous strain[31] between the strain in the equivalent homogeneous composite ε and the strain $\varepsilon_{i=1...k}$ in each layer is applied so that $\varepsilon = \varepsilon_{i=1...k}$. The effective Young's modulus of the equivalent homogeneous composite is then obtained as the arithmetic mean of the layers Young's moduli $\mathcal{E}_i$ weighted with their heights h_i, so that

$$\widehat{\mathcal{E}}_{eff}^{\parallel} = \frac{\sum\limits_{i=1}^{k} h_i \mathcal{E}_i}{\sum\limits_{i=1}^{k} h_i}, \tag{6}$$

with $h = \sum_{i=1}^{k} h_i$ being the height of the equivalent homogeneous composite. Equation (6) is independent of the layer order in the parallel stack.

Specimens with combined ($\perp\parallel$) stacking [e.g., in Fig. 2(c)] contain both serial and parallel stacked layers. The effective Young's modulus of the equivalent homogeneous composite $\mathcal{E}_{eff}^{\perp\parallel}$ of specimens with combined stacking is then modeled using first Eq. (6) to homogenize parallel stacked layers followed by applying Eq. (5) to the remaining equivalent stack of serial layers. As layers with high $\mathcal{E}_i$ contribute more to the arithmetic mean [Eq. (5) in $\widehat{\mathcal{E}}_{eff}^{\parallel}$] than to the harmonic mean [Eq. (6) in $\widehat{\mathcal{E}}_{eff}^{\perp}$], the subsequent steps in the homogenization procedure of the layer stack (from combined stacking to equivalent serial stack to homogeneous equivalent) cannot be permuted.

Inclusions associated with type A, type B, type C, and type D in Fig. 4 result in serial ($\perp$) or combined ($\perp\parallel$) stacked layers as summarized in Table II. The effective Young's modulus $\widehat{\mathcal{E}}_{eff}$ of the molded specimens from these types are, thus, modeled as $\widehat{\mathcal{E}}_{eff} = \widehat{\mathcal{E}}_{eff}^{\perp}$ or $\widehat{\mathcal{E}}_{eff} = \widehat{\mathcal{E}}_{eff}^{\perp\parallel}$. Following this model approach, shifting the same inclusion from the side to the center of the superficial layer does not affect the model outcome. Thus, $\widehat{\mathcal{E}}_{eff}$ for type A and type B specimens containing an inclusion with the same height ratio h_{in}/h have equal value. Indeed, as $\mathcal{E}_i$ are similar, modeled $\widehat{\mathcal{E}}_{eff}$ depends solely on the height ratio $0 \leq h_{in}/h \leq 1$ and length ratio $0 \leq l_{in}/l_2 \leq 1$ of the inclusion and not on its position. The influence of h_{in}/h and l_{in}/l_2 on $\widehat{\mathcal{E}}_{eff}$ is illustrated in Fig. 8. Model values for molded specimens are indicated (symbols). Extending the size of the inclusion in the superficial layer increases modeled $\widehat{\mathcal{E}}_{eff}$ from $\widehat{\mathcal{E}}_{eff} = 10$ kPa for the reference specimen $A_{0.0}$ without inclusion up to about $\widehat{\mathcal{E}}_{eff} = 33$ kPa for specimen $A_{1.0}$, for which the inclusion occupies the entire superficial layer. Nevertheless, Fig. 8(a) shows that $\widehat{\mathcal{E}}_{eff}$ increases more rapidly with l_{in}/l_2 than with h_{in}/h. In particular, this is the case for $h_{in}/h \geq 0.2$. This is due to the arithmetic mean associated with parallel stacked layers in Eq. (6), which tends to mask low $\mathcal{E}_i$ in favor of the large $\mathcal{E}_i$ of the inclusion (Table I), which is not the case for the harmonic mean associated with serial stacking in Eq. (5). Therefore, it is mainly the length ratio l_{in}/l_2 of the inclusion in the superficial layer what affects the mean value
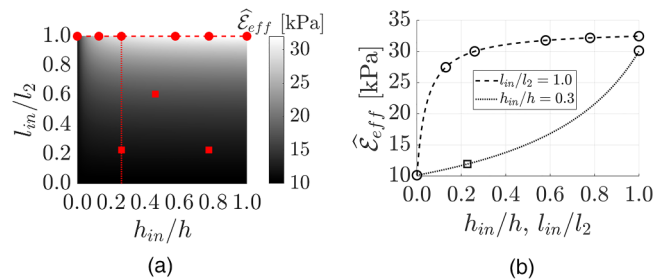

FIG. 8. Influence of the height ratio $0 \leq h_{in}/h \leq 1$ and length ratio $0 \leq l_{in}/l_2 \leq 1$ of an inclusion in the superficial layer on modeled $\widehat{\mathcal{E}}_{eff}$. Values for molded specimens ($\bigcirc$, $\square$) are shown: (a) specimens type A (or B) ($\bigcirc$) and type D ($\square$), constant length ratio $l_{in}/l_2 = 1.0$ (horizontal dashed line), and constant height ratio $h_{in}/h = 0.3$ (dashed vertical line); (b) detail for these constant length and height ratios. (a) varied l_{in}/l_2 and h_{in}/h; (b) constant l_{in}/l_2 or h_{in}/h.

$\widehat{\mathcal{E}}_{eff}^{\parallel}$ of the equivalent homogenized superficial layer and, hence, $\widehat{\mathcal{E}}_{eff}$ of the homogenized specimen. This is further illustrated for $l_{in}/l_2 = 1$ in Fig. 8(b) as an increase in h_{in}/h from 0.1 to 1 only increases $\widehat{\mathcal{E}}_{eff}$ 27%, from 26 up to 33 kPa, whereas for constant $h_{in}/h > 0.2$ ($h_{in}/h = 0.3$ is plotted) an increase in l_{in}/l_2 from 0.1 to 1 increases $\widehat{\mathcal{E}}_{eff}$ with about 270% from 11 up to 30 kPa. Thus, the most notable variation of $\widehat{\mathcal{E}}_{eff}$ for the molded specimens plotted in Fig. 8(a) is predicted to occur for specimens with different inclusion lengths $l_{in}/l_2 \in \{0.0, 0.2, 0.6, 1\}$ associated with $\widehat{\mathcal{E}}_{eff} \in \{10, 12, 17, 30\}$ kPa.

B. Arbitrary layer stacking

Specimens of type E with an inclined inclusion ($\alpha > 0°$) in the superficial layer [Fig. 4(e)] or of type F with a bent inclusion in the muscle layer [Fig. 4(f)] are not serial or parallel stacked with respect to adjacent layers. Instead, their stacking is arbitrary (Arb). However, using the model outlined in Sec. IV A for serial, parallel, and combined stacking, two approaches are proposed to model the effective Young's modulus $\widehat{\mathcal{E}}_{eff}$ for arbitrary stacked layers based either on spatial discretization along the force direction (Sec. IV B 1) or on geometrical approximation (Sec. IV B 2). A comparison of modeled values with both approaches for molded specimens with arbitrary stacking $E_{0.5}^{0.6}$ and $F_{0.3}$ is provided in Sec. IV B 3.

1. Discretization

The model approach outlined in Sec. IV A is applied to arbitrary stacking by discretizing the specimen portion containing the inclusion with equivalent length l_{eq} into multiple shorter layers

with discretization step length l_j. The inclusion within each discretized layer is then approximated by a rectangle with height h_j set either to height h_j^U of the largest rectangle enveloped within the inclusion or to height h_j^O of the smallest rectangle enveloping the inclusion in that discretized layer as schematically depicted in Fig. 9 for specimens of type E and type F. Consequently, each discretized layer with rectangular inclusion approximation is represented as parallel stacked layers so that $\widehat{\mathcal{E}}_{eff,j}$ of each homogenized discretized layer is modeled using Eq. (6). The sought $\widehat{\mathcal{E}}_{eff,j}$ of each discretized layer with length l_j is, thus, underestimated (U) as $\widehat{\mathcal{E}}_{j,U} = \widehat{\mathcal{E}}_{eff}^{\parallel}$ using height h_j^U or overestimated (O) as $\widehat{\mathcal{E}}_{j,O} = \widehat{\mathcal{E}}_{eff}^{\parallel}$ using height h_j^O. Following this discretization, the equivalent homogenized specimen portion with inclusion and, therefore, the equivalent homogenized specimen consist of a stack of serial layers, so that $\widehat{\mathcal{E}}_{eff}$ is modeled using Eq. (5) resulting in overestimation $\widehat{\mathcal{E}}_O = \widehat{\mathcal{E}}_{eff}^{\perp}$ for $\widehat{\mathcal{E}}_{j,O}$ or in underestimation $\widehat{\mathcal{E}}_U = \widehat{\mathcal{E}}_{eff}^{\perp}$ for $\widehat{\mathcal{E}}_{j,U}$. The overall difference $\widehat{\mathcal{E}}_O - \widehat{\mathcal{E}}_U \geq 0$ for the equivalent homogenized specimen portion with inclusion of length l_{eq} [Figs. 10(c) and 10(d)] and for the equivalent homogenized specimen [Figs. 10(e) and 10(f)] decreases with discretization step length l_j. Consequently, the sought model value $\widehat{\mathcal{E}}_{eff}$ of the homogenized specimen is found for small enough discretization step length l_j. The influence of the discretization step length l_j is illustrated in Fig. 10 for molded specimen $E_{0.5}^{0.6}$ containing an inclined inclusion with $l_{eq} = 15.7$ mm [type E in Fig. 4(f)] and for molded specimen $F_{0.3}$ containing a bent inclusion with $l_{eq} = 10.2$ mm [type F in Fig. 4(e)]. For these specimens, $\widehat{\mathcal{E}}_{eff}$ of both the equivalent homogeneous inclusion layer (with length l_{eq}) and of the specimen is approximated when the discretization step length $l_j \leq 0.2$ mm as
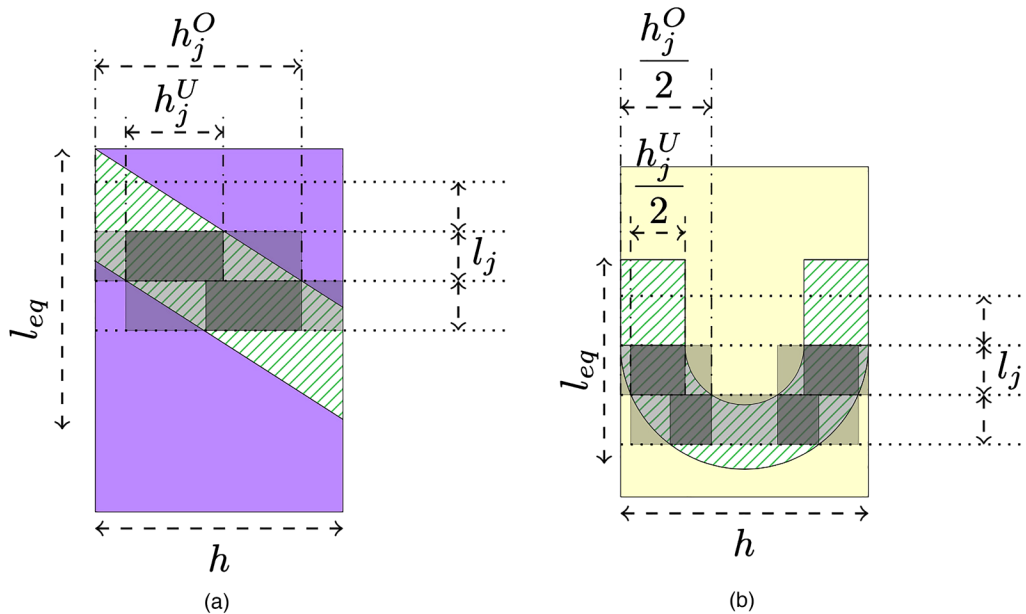

FIG. 9. Illustration of discretization along the force direction (step length l_j) for inclusions (striped region) with arbitrary stacking: (a) type E (specimen $E_{0.5}^{0.6}$); (b) type F (specimen $F_{0.3}$). Rectangular inclusion portion approximations with height h_j^O (light gray shade) and h_j^U (dark gray shade) overestimating (O) and underestimating (U) the inclusion, respectively. (a) Type E, specimen $E_{0.5}^{0.6}$; (b) type F, specimen $F_{0.3}$.
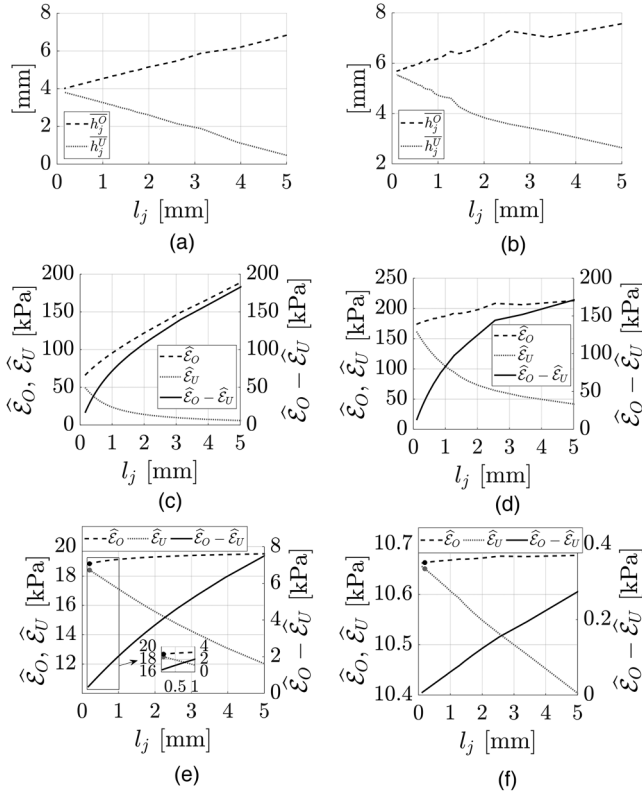
FIG. 10. Effect of discretization step length l_j for molded ML specimens $E_{0.5}^{0.6}$ and $F_{0.3}$ on (a) and (b) mean rectangle heights $\overline{h_j^O}(l_j)$ and $\overline{h_j^U}(l_j)$, (c) and (d) modeled effective Young's modulus $\widehat{\mathcal{E}}_O(l_j, h_j^O)$ and $\widehat{\mathcal{E}}_U(l_j, h_j^U)$ and the difference $\widehat{\mathcal{E}}_O - \widehat{\mathcal{E}}_U$ for the homogenized specimen portion with an inclusion of length l_{eq}, and (e) and (f) modeled effective Young's modulus $\widehat{\mathcal{E}}_O(l_j, h_j^O)$ and $\widehat{\mathcal{E}}_U(l_j, h_j^U)$ and the difference $\widehat{\mathcal{E}}_O - \widehat{\mathcal{E}}_U$ for the homogenized specimen. Values of $\widehat{\mathcal{E}}_{O,U}$ for $l_j = 0.2$ mm are indicated (●). (a) Specimen $E_{0.5}^{0.6}$, (b) specimen $F_{0.3}$, (c) Eq. layer $l_{eq} = 16.6$ mm of $E_{0.5}^{0.6}$, (d) Eq. layer $l_{eq} = 10.2$ mm of $F_{0.3}$, (e) specimen $E_{0.5}^{0.6}$, and (f) specimen $F_{0.3}$.

$\widehat{\mathcal{E}}_O - \widehat{\mathcal{E}}_U \le 0.5$ kPa for both homogenized specimens. For $l_j = 0.2$ mm, the discretization of l_{eq} corresponds to splitting l_{eq} into 78 ($E_{0.5}^{0.6}$) and 51 ($F_{0.3}$) equi-length layers. It is seen from Figs. 10(a) and 10(b) that also the mean of rectangle heights for all discretized layers $\overline{h_j^O}$ and $\overline{h_j^U}$ converges as l_j decreases.

2. Geometrical approximation

Besides the discretization approach outlined in Sec. IV B 1, the quasi-analytical model approach outlined in Sec. IV A can be applied when the inclusion of height h_{in} and length l_{in} with arbitrary stacking can be treated as an equivalent beam-shaped inclusion of length l_{eq} and height h_{eq} with serial, parallel, or combined layer stacking. The length l_{eq} corresponds to the equivalent length of the inclusion in the force direction as illustrated for type E and type F specimens in Figs. 4 and 9. The height h_{eq} of the equivalent inclusion is obtained when imposing area conservation and

exploiting the model property that neither serial [Eq. (5)] or parallel [Eq. (6)] layer stacks depend on the stack order so that layers in both stacks can be split or permuted. The area conservation condition is defined as $h_{in}l_{in} = h_{eq}l_{eq}$, so that

$$h_{eq} = \frac{h_{in}l_{in}}{l_{eq}}. \qquad (7)$$

The dimensions of the equivalent inclusions h_{eq} and l_{eq} can then be expressed in terms of geometrical parameters such as inclusion dimensions h_{in} and l_{in}.

For specimens of type E, such as $E_{0.5}^{0.6}$ containing an inclined inclusion as depicted in Fig. 4(e), l_{eq} and h_{eq} are expressed as

$$
\begin{aligned}
l_{eq} &= \frac{h_{in} + h\cos(\alpha)}{\sin(\alpha)}, \\
h_{eq} &= \frac{l_{in}h_{in}\sin(\alpha)}{h_{in} + h\cos(\alpha)}.
\end{aligned}
\qquad (8)
$$

For specimens of type F, such as $F_{0.3}$ containing a bent inclusion as depicted in Fig. 4(f), l_{eq} and h_{eq} are given as

$$
\begin{aligned}
l_{eq} &= \frac{l_{in} + h}{2} - \frac{\pi(h - h_{in})}{4}, \\
h_{eq} &= \frac{4h_{in}l_{in}}{2l_{in} + \pi h_{in} - (\pi - 2)h}.
\end{aligned}
\qquad (9)
$$

Analytical expressions of the geometry of equivalent inclusions, such as Eqs. (8) and (9), are of interest when considering the influence of geometrical inclusion parameters on $\widehat{\mathcal{E}}_{eff}$. As an additional example (not molded), expressions of the equivalent length l_{eq} and height h_{eq} of an inclusion with inclination angle α fully embedded in the superficial layer, i.e., with a diagonal shorter than
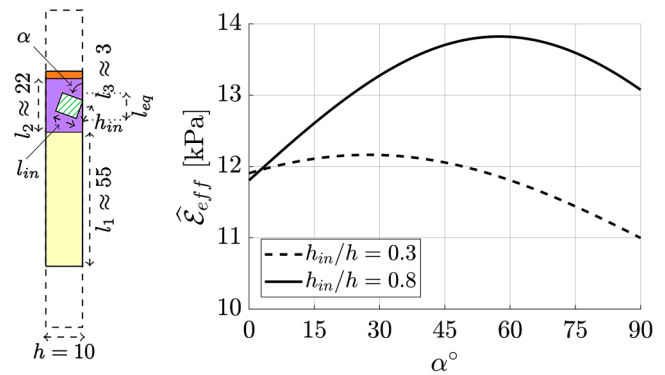

FIG. 11. Modeled $\widehat{\mathcal{E}}_{eff}$ as a function of inclination angle α ($0° \le \alpha \le 90°$) for specimens with an embedded inclusion of diagonal $\sqrt{l_{in}^2 + h_{in}^2} \le h$ as schematically depicted (left). Curves $\widehat{\mathcal{E}}_{eff}(\alpha)$ are plotted for $l_{in}/l_2 = 0.2$ and either $h_{in}/h = 0.3$ (dashed line) or $h_{in}/h = 0.8$ (full line).
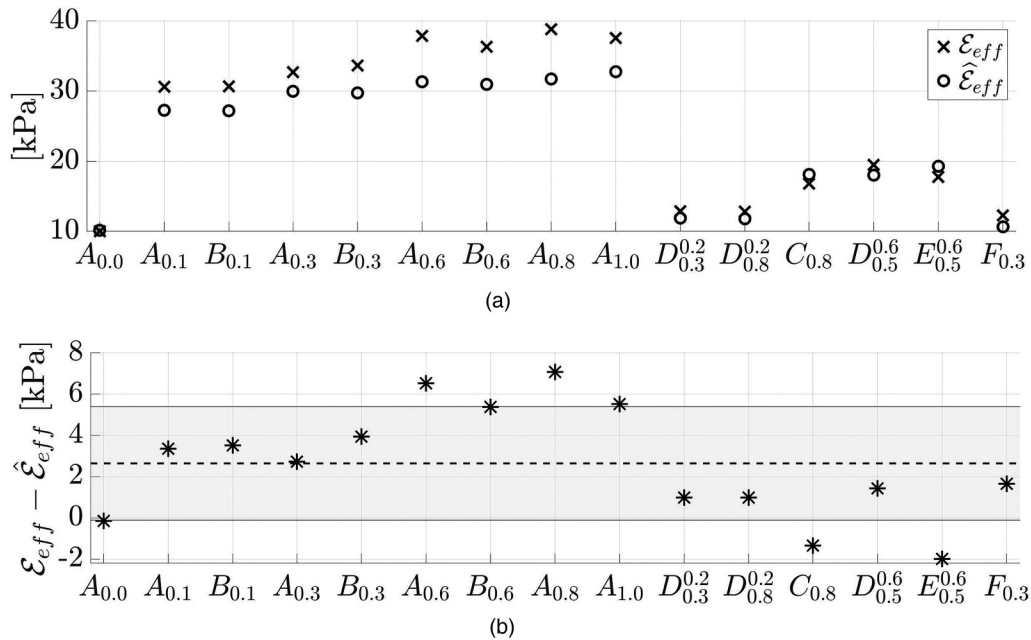
FIG. 12. Low-strain Young's moduli for molded ML specimens: (a) Measured $\mathcal{E}_{eff}$ ($\times$) and modeled $\widehat{\mathcal{E}}_{eff}$ ($\circ$). (b) Difference $\mathcal{E}_{eff} - \widehat{\mathcal{E}}_{eff}$ ($*$) with the overall mean (dashed line) and standard deviation (shaded area).

the total specimen height h so that $\sqrt{l_{in}^2 + h_{in}^2} \leq h$ as schematically depicted in Fig. 11, are

$$l_{eq} = l_{in}\cos(\alpha) + h_{in}\sin(\alpha),$$
$$h_{eq} = \frac{l_{in}h_{in}}{l_{in}\cos(\alpha) + h_{in}\sin(\alpha)}. \qquad (10)$$

Modeled $\widehat{\mathcal{E}}_{eff}$ for two fully embedded inclined inclusions from Table II, with length $l_{in} = 5.0\,\text{mm}$ (or $l_{in}/l_2 = 0.2$) and height $h_{in} \in \{2.6\,\text{mm}, 7.8\,\text{mm}\}$ (or $h_{in}/h \in \{0.3, 0.8\}$), as a function of inclination angle $0° \leq \alpha \leq 90°$ is plotted in Fig. 11. Although the overall tendency of $\widehat{\mathcal{E}}_{eff}(\alpha)$ is similar, plotted curves show, e.g., that angles associated with the minimum and maximum of the curves depend on the height ratio h_{in}/h.

3. $\widehat{\mathcal{E}}_{eff}$ of molded specimens with arbitrary stacking

For the molded specimens with arbitrary stacking, both the discretization approach (in Sec. IV B 1 with step length $l_j = 0.2\,\text{mm}$) and the geometrical approximation approach (in Sec. IV B 2) result in the sought $\widehat{\mathcal{E}}_{eff}$ as their difference is less than $0.9\,\text{kPa}$ (or $\leq 4.8\%$) for specimen $E_{0.5}^{0.6}$ and less than $0.1\,\text{kPa}$ (or $\leq 1.0\%$) for specimen $F_{0.3}$. Hereafter, $\widehat{\mathcal{E}}_{eff}$ obtained with the geometrical approximation is reported for specimens with arbitrary stacked inclusions ($E_{0.5}^{0.6}$ and $F_{0.3}$) since in this case $\widehat{\mathcal{E}}_{eff}$ does not depend on the applied discretization step length l_j.

V. MODELLED $\widehat{\mathcal{E}}_{eff}$ vs MEASURED $\mathcal{E}_{eff}$

The model approach outlined in Sec. IV is next used to predict the low-strain $\widehat{\mathcal{E}}_{eff}$ of each of the 15 molded specimens. Modeled $\widehat{\mathcal{E}}_{eff}$ and measured $\mathcal{E}_{eff}$ values are plotted in Fig. 12(a). The difference $\mathcal{E}_{eff} - \widehat{\mathcal{E}}_{eff}$ between measured and modelled values is plotted in Fig. 12(b). The absolute value $|\mathcal{E}_{eff} - \widehat{\mathcal{E}}_{eff}|$ for specimens with inclusions corresponds to a model error ranging from 1.0 up to 7.1 kPa, which amounts to 7.4% up to 18.3% of the measured $\mathcal{E}_{eff}$. Overall $\mathcal{E}_{eff} - \widehat{\mathcal{E}}_{eff}$ of molded specimens is characterized by a mean (and standard deviation) of 2.7 (2.7) kPa. Compared to the overall model accuracy of 0.0 (2.4) kPa obtained for two- and three-layer specimens reported in Ref. 10, the overall model accuracy for specimens with inclusions is, thus, shifted due to the non-zero mean to the range from 0.0 up to 5.2 kPa. The positive non-zero mean of 2.7 kPa indicates that the model tends to underestimate measured values. From Fig. 12, it is seen that the underestimation (with 2.7 up to 7.1 kPa) is associated with specimens of type A and type B for which the influence of the inclusion on Young's modulus is most prominent as their measured effective Young's modulus ($\mathcal{E}_{eff} \geq 30.6\,\text{kPa}$) is at least tripled compared to $\mathcal{E}_{eff} = 10.2\,\text{kPa}$, measured for the reference specimen without inclusion $A_{0.0}$. Despite this underestimation, the measured $\mathcal{E}_{eff}$ and modeled $\widehat{\mathcal{E}}_{eff}$ values exhibit the same tendencies so that the experimental data validate the model approach for all specimen types (including the ones with arbitrary stacking) and also the model properties discussed in Sec. IV such as:

- Comparing measured $\mathcal{E}_{eff}$ for specimens of type A (inclusion at the side) and type B (inclusion at the center) confirms that the
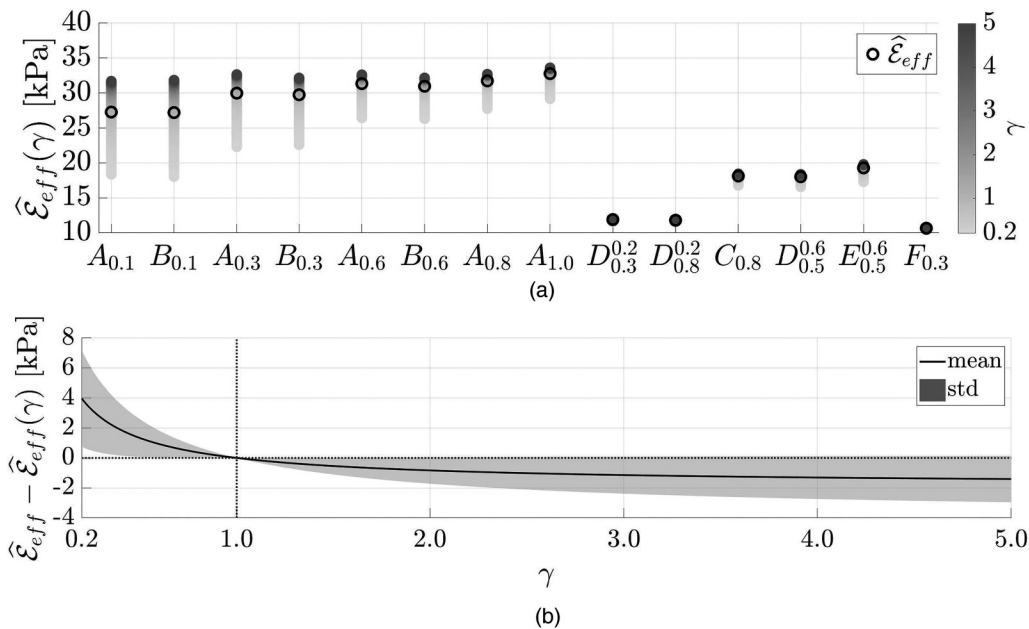
FIG. 13. Effect of scaling Young's modulus of the inclusion $\mathcal{E}^{In}$ with a scalar $0.2 \leq \gamma \leq 5$ on modeled $\widehat{\mathcal{E}}_{eff}(\gamma)$ for all 14 ML composite types with inclusion: (a) $\widehat{\mathcal{E}}_{eff}(\gamma)$ for increasing $0.2 \leq \gamma \leq 5$ (gray scale) and $\widehat{\mathcal{E}}_{eff}$ for $\gamma = 1$ (○) and (b) overall mean (full line) and standard deviation (std, shaded region) of $\widehat{\mathcal{E}}_{eff} - \widehat{\mathcal{E}}_{eff}(\gamma)$. As a reference, dotted lines indicate zero difference (horizontal) and $\gamma = 1$ (vertical). (a) $\widehat{\mathcal{E}}_{eff}(\gamma)$ (gray scale), $\widehat{\mathcal{E}}_{eff}$ for $\gamma = 1$ (○); (b) mean and standard deviation of $\widehat{\mathcal{E}}_{eff} - \widehat{\mathcal{E}}_{eff}(\gamma)$.

transverse position of the inclusion within the superficial layer does not affect the effective Young's modulus of the specimen as the difference between $\mathcal{E}_{eff}$ measured for $A_{h_{in}/h}$ and $B_{h_{in}/h}$ is less than 1.6 kPa for all three assessed h_{in}/h ratios (0.1, 0.3, 0.6).

- Comparing measured $\mathcal{E}_{eff}$ for specimens of type A (inclusion with $l_{in}/l_2 = 1$) and type D (inclusion with $l_{in}/l_2 = 0.2$) confirms the influence of the inclusion size (length l_{in}/l_2 and height h_{in}/h ratios) on the modeled $\widehat{\mathcal{E}}_{eff}$ shown in Fig. 8 so that in particular the length of the inclusion in the force direction (l_{in}/l_2) affects the effective Young's modulus $\mathcal{E}_{eff}$ for these specimens.
- Comparing measured $\mathcal{E}_{eff}$ for specimens $A_{0.8}$ (type A, inclusion in the superficial layer) and $C_{0.8}$ (type C, inclusion in both the superficial and the muscle layers) confirms that the influence of the inclusion on measured $\mathcal{E}_{eff}$ increases with Young's modulus ratio $\mathcal{E}^{in}/\mathcal{E}$, which for the molded specimens (Table I) reduces from 74.5 in the superficial layer to 4.6 in the muscle layer.

The influence of the ratio $\mathcal{E}^{In}/\mathcal{E}$ is further explored using the model. Young's modulus of the inclusion $\mathcal{E}^{In}$ and Young's modulus ratio $\mathcal{E}^{In}/\mathcal{E}$ of the superficial and muscle layers given in Table I are scaled as $\gamma \mathcal{E}^{In}$. The scalar γ is varied between 0.2 ($\mathcal{E}^{In}$ divided by 5) and 5 ($\mathcal{E}^{In}$ multiplied by 5) so that unscaled model values $\widehat{\mathcal{E}}_{eff}$ for $\mathcal{E}^{In}$ are obtained for $\gamma = 1$. In particular, the scaled Young's modulus of the inclusion $\gamma \mathcal{E}^{In}$ ranges from 60 kPa up to 1.49 MPa so that the associated Young's modulus ratios $\mathcal{E}^{In}/\mathcal{E}$ for the superficial layer (ratio from 14.9 up to 372) and for the muscle layer (ratio from 2.6 up to 65) containing the inclusion remain greater than 1 (so an inclusion is embedded in a softer layer). Modeled $\widehat{\mathcal{E}}_{eff}(\gamma)$ for all 14 composite types with inclusion is plotted in Fig. 13(a). Values $\widehat{\mathcal{E}}_{eff}$ (circles) for $\gamma = 1$ obtained for the molded specimens are indicated as a reference. For each composite type, $\widehat{\mathcal{E}}_{eff}(\gamma)$ increases with γ. Values of $\widehat{\mathcal{E}}_{eff}(\gamma)$ for $\gamma \in \{0.2, 1.0, 5.0\}$ and the relative maximum difference (in %) of $\widehat{\mathcal{E}}_{eff}(\gamma)$ with respect to $\widehat{\mathcal{E}}_{eff}$

TABLE III. Influence of scaling inclusions Young's modulus $\mathcal{E}^{In}$ with scalar $\gamma \in \{0.2, 1, 5\}$ on modelled $\widehat{\mathcal{E}}_{eff}$ (in kPa) for all 14 composite types with inclusion and the relative maximum difference $\mathcal{D}$ (in %) with respect to $\widehat{\mathcal{E}}_{eff}$ for $\gamma = 1$.

γ	$A_{0.1}$	$B_{0.1}$	$A_{0.3}$	$B_{0.3}$	$A_{0.6}$	$B_{0.6}$	$A_{0.8}$	$A_{1.0}$	$D_{0.3}^{0.2}$	$D_{0.8}^{0.2}$	$C_{0.8}$	$D_{0.5}^{0.6}$	$E_{0.5}^{0.6}$	$F_{0.3}$
0.2	18.4	18.0	22.3	22.6	26.4	26.3	27.8	29.2	11.6	11.7	16.8	16.6	17.3	10.4
1.0	27.3	27.2	30.0	29.8	31.3	31.0	31.7	32.8	11.9	11.8	18.1	18.0	19.3	10.7
5.0	31.7	31.8	32.6	32.2	32.6	32.2	32.7	33.6	12.0	11.8	18.4	18.4	19.8	10.7
$\mathcal{D}$	49	51	34	32	20	19	15	13	3	1	9	10	13	3

for $\gamma = 1$

$$\mathcal{D} = \frac{\widehat{\mathcal{E}}_{eff}(5) - \widehat{\mathcal{E}}_{eff}(0.2)}{\widehat{\mathcal{E}}_{eff}} \qquad (11)$$

are summarized in Table III. The relative maximum difference $\mathcal{D}$ ranges from 1% up to 51%. As observed in Fig. 13(a), the influence of scaling Young's modulus of the inclusion on $\widehat{\mathcal{E}}_{eff}$ depends on the composite type. The overall (for all composite types) mean and standard deviation (std) of the difference $\widehat{\mathcal{E}}_{eff} - \widehat{\mathcal{E}}_{eff}(\gamma)$ as a function of γ are plotted in Fig. 13(b). Both the mean and std become zero at $\gamma = 1$ for which the difference is zero by definition (since $\widehat{\mathcal{E}}_{eff} = \widehat{\mathcal{E}}_{eff}(\gamma = 1)$). As $\widehat{\mathcal{E}}_{eff}(\gamma)$ increases with γ, the overall mean of $\widehat{\mathcal{E}}_{eff} - \widehat{\mathcal{E}}_{eff}(\gamma)$ decreases monotonically as γ increases. Thus, the overall mean difference is positive for $\gamma < 1$ and negative for $\gamma > 1$ since $\widehat{\mathcal{E}}_{eff} > \widehat{\mathcal{E}}_{eff}(\gamma < 1)$ and $\widehat{\mathcal{E}}_{eff} < \widehat{\mathcal{E}}_{eff}(\gamma > 1)$. The rate at which the overall mean difference decreases slows down with γ. The model suggests that for the assessed composite types, $\widehat{\mathcal{E}}_{eff}$ becomes less sensitive to the exact value of $\mathcal{E}^{In}$ for large $\mathcal{E}^{In}/\mathcal{E}$ ratios. The overall standard deviation of $\widehat{\mathcal{E}}_{eff} - \widehat{\mathcal{E}}_{eff}(\gamma)$ increases with $|\gamma - 1|$, which expresses that the influence of scaling $\mathcal{E}^{In}$ on $\widehat{\mathcal{E}}_{eff}$ differs between composite types.

VI. CONCLUSION

The effective low-strain elastic Young's modulus of silicone ML composites is measured on 15 molded bone-shaped specimens using uni-axial stress testing. A reference specimen is obtained from a three-layer vocal fold anatomical representation of the muscle, superficial, and epithelium layers with Young's modulus between 4 and 65 kPa. More complex ML composite types with at least four layers are obtained by embedding a stiffer (298 kPa) inclusion with variable size, position, and stacking in the superficial or/and muscle layer of the reference specimen. Measured effective Young's moduli of all 15 molded ML composite specimens are compared to modeled values describing equivalent homogenized specimens based on the geometry of their layers, Young's moduli, and stacking. For ML specimens consisting solely of serial and/or parallel stacked layers, an analytical model approach is applied, which exploits the hypothesis of homogeneous strain for parallel stacked layers and the hypothesis of homogeneous stress for serial stacked layers. A model approach is proposed for specimens for which the inclusion results in arbitrary stacking, first using spatial discretization along the force direction and then using area conservation to propose a geometrical approximation for inclined or bent inclusions. Modeled effective Young's moduli are validated against measured values (from 10 up to 40 kPa), resulting in an overall model accuracy between 0.0 and 5.2 kPa.

The validated quasi-analytical model allows one to explore the influence of its parameters on the predicted effective Young's modulus. Concretely, the influence of the dimensions of an inclusion in the superficial layer and the influence of scaling the Young's modulus of the inclusion for different ML composite types are discussed. In the first case, the length of the inclusion in the force direction is shown to determine the modeled effective Young's modulus, whereas in the latter case it was found that the rate at which the effective Young's modulus increases with the

inclusions slows down, so that eventually for stiff inclusions the exact value of its Young's modulus becomes less important. It is expected that the proposed model and subsequent model parameter studies are of interest for the *a priori* characterization and design of silicone ML composite vocal fold replicas mimicking the complex ML anatomical vocal fold structure without or with inclusion, as in the case of a structural pathology or abnormality. Therefore, the current results are important considering the understanding and the mitigation of structural pathologies entraining local vocal fold stiffening and their potential impact on human voice production.

AUTHOR DECLARATIONS

Conflict of Interest

There are no conflicts of interest to disclose.

DATA AVAILABILITY

The data the support the findings of this study are available from the corresponding author upon reasonable request.

REFERENCES

[1]C. Rosen and C. Simpson, *Operative Techniques in Laryngology* (Springer-Verlag, 2008).

[2]N. Ruty, X. Pelorson, A. Van Hirtum, I. Lopez, and A. Hirschberg, "An *in-vitro* setup to test the relevance and the accuracy of low-order models of the vocal folds," J. Acoust. Soc. Am. **121**, 479–490 (2007).

[3]J. Lucero, A. Van Hirtum, N. Ruty, J. Cisonni, and X. Pelorson, "Validation of theoretical models of phonation threshold pressure with data from a vocal fold mechanical replica," J. Acoust. Soc. Am. **125**, 632–635 (2009).

[4]J. Cisonni, A. Van Hirtum, X. Pelorson, and J. Lucero, "The influence of geometrical and mechanical input parameters on theoretical models of phonation," Acta Acustica **97**, 291–302 (2011).

[5]P. Luizard and X. Pelorson, "Threshold of oscillation of a vocal folds replica with unilateral surface growths," J. Acoust. Soc. Am. **141**, 3050–3058 (2017).

[6]J. Lucero, X. Pelorson, and A. Van Hirtum, "Phonation threshold pressure at large asymmetries of the vocal folds," Biomed. Sig. Proc. Control **62**, 102105 (2020).

[7]J. Cisonni, A. Van Hirtum, X. Pelorson, and J. Willems, "Theoretical simulation and experimental validation of inverse quasi one-dimensional steady and unsteady glottal flow models," J. Acoust. Soc. Am. **124**, 535–545 (2008).

[8]B. Fabre, J. Gilbert, A. Hirschberg, and X. Pelorson, "Aeroacoustics of musical instruments," Ann. Rev. Fluid Mech. **44**, 1–25 (2012).

[9]R. Mittal, B. Erath, and M. Plesniak, "Fluid dynamics of human phonation and speech," Ann. Rev. Fluid Mech. **45**, 437–467 (2013).

[10]M. Ahmad, A. Bouvet, X. Pelorson, and A. Van Hirtum, "Modeling and validation of the elasticity parameters of multi-layer specimens pertinent to silicone vocal fold replicas," Int. J. Mech. Sci. **208**, 106685 (2021).

[11]B. Pickup and S. Thomson, "Flow-induced vibratory response of idealized versus magnetic resonance imaging-based synthetic vocal fold models," J. Acoust. Soc. Am. **128**, EL124–EL129 (2010).

[12]P. Murray and S. Thomson, "Synthetic, multi-layer, self-oscillating vocal fold model fabrication," J. Vis. Exp. **58**, e3498 (2011).

[13]P. Murray and S. Thomson, "Vibratory responses of synthetic, self-oscillating vocal fold models," J. Acoust. Soc. Am. **132**, 3428–3438 (2012).

[14]I. Tokuda and R. Shimamura, "Effect of level difference between left and right vocal folds on phonation: Physical experiment and theoretical study," J. Acoust. Soc. Am. **142**, 482–492 (2017).

[15]R. Shimamura and I. T. Tokuda, "Experimental study on level difference between left and right vocal folds," Acoust. Sci. Technol. **38**, 264–267 (2017).

[16]A. Bouvet, I. Tokuda, X. Pelorson, and A. Van Hirtum, "Influence of level difference due to vocal folds angular asymmetry on auto-oscillating replicas," J. Acoust. Soc. Am. **147**, 1136–1145 (2020).

[17]A. Bouvet, I. Tokuda, X. Pelorson, and A. Van Hirtum, "Imaging of auto-oscillating vocal folds replicas with left-right level difference due to angular asymmetry," Biomed. Sig. Proc. Control **63**, 102154 (2021).

[18]A. Van Hirtum, A. Bouvet, I. Tokuda, and X. Pelorson, "Dynamic vibration mode decomposition of auto-oscillating vocal fold replicas without and with vertical tilting," J. Sound Vibr. **516**, 1–11 (2021).

[19]M. Hirano, S. Kurita, and T. Nakashima, *Vocal Fold Physiology* (College Hill Press, 1983), pp. 22–43.

[20]F. Alipour and I. Titze, "Elastic models of vocal fold tissues," J. Acoust. Soc. Am. **90**, 1326–1331 (1991).

[21]Y. Min, I. Titze, and F. Alipour, "Stress-strain response of the human vocal ligament," Ann. Otol. Rhinol. Laryngol **104**, 563–569 (1995).

[22]R. Chan, M. Fu, L. Young, and N. Tirunagari, "Relative contributions of collagen and elastin to elasticity of the vocal fold under tension," Ann. Biomed. Eng. **35**, 1471–1483 (2007).

[23]A. Miri, "Mechanical characterization of vocal fold tissue: A review study," J. Voice **28**, 657–667 (2014).

[24]D. Chhetri, Z. Zhang, and J. Neubauer, "Measurement of Young's modulus of vocal folds by indentation," J. Voice **25**, 1–7 (2011).

[25]Z. Zhang, H. Samajder, and J. Long, "Biaxial mechanical properties of human vocal fold cover under fold elongation," J. Acoust. Soc. Am. **29**, EL356 (2017).

[26]J. K. Hansen and S. L. Thibeault, "Current understanding and review of the literature: Vocal fold scarring," J. Voice **20**, 110–120 (2006).

[27]G. Friedrich, F. G. Dikkers, C. Arens, M. Remacle, M. Hess, A. Giovanni, S. Duflo, A. Hantzakos, V. Bachy, and M. Gugatschka, "Vocal fold scars: Current concepts and future directions. consensus report of the phonosurgery committee of the european laryngological society," Eur. Arch. Otorhinolaryngol. **270**, 2491–2507 (2013).

[28]A. Mattei, J. Magalon, B. Bertrand, C. Philandrianos, J. Véran, and A. Giovanni, "Cell therapy and scarred vocal folds," Eur. Ann. Otorhinolaryngol. **134**, 339–345 (2017).

[29]A. Bouvet, "Experimental and theoretical contribution to the analysis and the modelling of the vocal folds vibration," Ph.D. thesis (Grenoble Alpes University, 2019).

[30]A. Reuss, "Berechnung der fließgrenze von mischkristallen auf grund der plastizitätsbedingung für einkristalle," ZAMM **9**, 49–58 (1929).

[31]W. Voigt, "Ueber die beziehung zwischen den beiden elasticitätsconstanten isotroper körper," Ann. Phys. **274**, 573–587 (1889).